ACS APPLIED MATERIALS & INTERFACES

Research Article

www.acsami.org

Na Insertion Mechanisms in Vanadium Oxide Nanotubes for Na-Ion Batteries

Hyunjin Kim, Dong Young Kim, Yongsu Kim, Seok-Soo Lee, and Kwangjin Park*

Samsung Advanced Institute of Technology (SAIT), Electronic Materials Research Complex, 130, Samsung-ro, Maetan-dong, Yeongtong-gu, Suwon-si, Gyeonggi-do 443-803, Republic of Korea

Supporting Information

ABSTRACT: In this study, we successfully synthesized lamellar-structured $Ni_{0.1}VO_x$ NTs by a microwave-assisted hydrothermal method and cation exchange reaction. High initial discharge capacity and 100% efficiency were obtained when the $Ni_{0.1}VO_x$ NTs cathode was used as a cathode material for the Na battery. The intercalation mechanism and capacity fading effect were investigated in detail both experimentally using Transmission electron microscopy (TEM), X-ray diffraction (XRD), Fourier transform infrared spectroscopy (FT-IR) and X-ray photoelectron spectroscopy (XPS) analyses and theoretically using the ab initio simulation method. During the intercalation of Na^+ into VO_x NT structures, TEM, XRD, FT-IR, and XPS data revealed the cointercalation of the solvent, resulting in the expansion of the interlayer spacing and carbon and oxygen adsorption. The experimental and simulation results suggest that solvent molecules coordinated the Na insertion mechanisms into the amine interlayer during discharging. These understandings of the Na intercalation mechanism in materials based on $Ni_{0.1}VO_x$ NTs would be useful to design more stable and high-performance VO_x-based electrodes for Na battery applications.

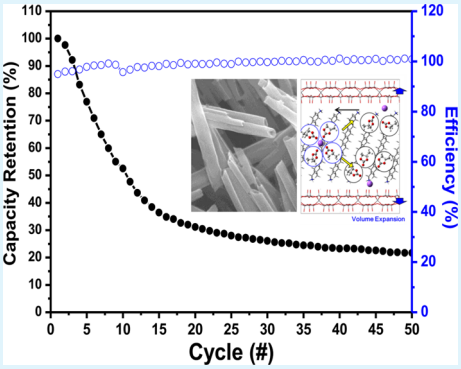

KEYWORDS: *Na battery, vanadium oxide nanotubes, Na insertion mechanism, cointercalation, Ni doping*

INTRODUCTION

In conjunction with the increased demand for renewable and sustainable energy sources, studies have extensively focused on developing next-generation batteries. In particular, "non-lithium batteries" in which Li^+ is substituted by Na^+[1−5] or Mg^{2+}[6] have attracted considerable interest for electricity storage system applications. Among these batteries, Na^+ batteries are considered especially promising because Na is a relatively abundant element in the earth, and the manufacturing cost of Na^+ batteries is relatively low.

Accordingly, many cathode materials have been developed for Na^+ batteries. For example, several groups have successfully demonstrated that layered transition metal oxides such as $NaxMO_2$, (M = Co, Ni, Cr, Fe, Mn) can be used as cathode materials for a Na^+ battery.[1−5,7] Layered vanadium oxide is considered one of the most promising materials because its layered structure facilitates mobile cation insertion and extraction within the layered framework.[8−11]

Because the volume of Na^+ is ∼70% higher than that of Li^+, a larger open framework is required to facilitate mobile cation insertion and extraction in the cathode materials. In this regard, many studies have recently attempted to increase the interlayer spacing and surface area of VO_x. For examples, Hamani et al. and Tepavcevic et al. attempted to improve the characteristics of vanadium oxide as a cathode material in Na^+ batteries.[8,9] Su and Wang reported that the electrochemical performance of Na^+ batteries could be improved by using bilayered V_2O_5.[10] Moreover, it has been found that vanadium oxides structured in the form of nanosheets,[11] nanobelts,[12] and nanoribbons[13] exhibit improved electrochemical performance because of their higher surface areas and short ion-migration pathways.

In particular, VO_x nanotubes (NTs) have recently attracted attention because they offer a large active surface area and numerous channels for ionic transport[14−19] owing to their multiwalled tubular structures. Moreover, the interlayer spacing can be easily modulated by using different amine templates with different numbers of carbon chains. Increased interlayer spacing via the amine templates will allow the facile electrochemical intercalation of mobile cations larger than Li^+, such as Mg^+ and Na^+. Recently, our previous study successfully demonstrated VO_x NTs and Ni-doped VO_x NTs as cathode materials for a Na^+ battery.[5] Ni-doped VO_x NTs exhibit relatively high initial capacity (143.6 mAh/g). However, the NTs show steeper capacity fading rate than other cathode materials.[5] Therefore, understanding the intercalation and degradation mechanisms is crucial for improving the electrochemical performance by engineering VO_x structures for Na^+ battery applications.[15−18]

In this study, we have successfully synthesized $Ni_{0.1}VO_x$ NTs using hydrothermal synthesis with a cationic exchange reaction and used them as cathode materials for a Na^+ battery. $Ni_{0.1}VO_x$

Received: September 4, 2014
Accepted: January 6, 2015
Published: January 6, 2015

DOI: 10.1021/am506051t
ACS Appl. Mater. Interfaces 2015, 7, 1477−1485

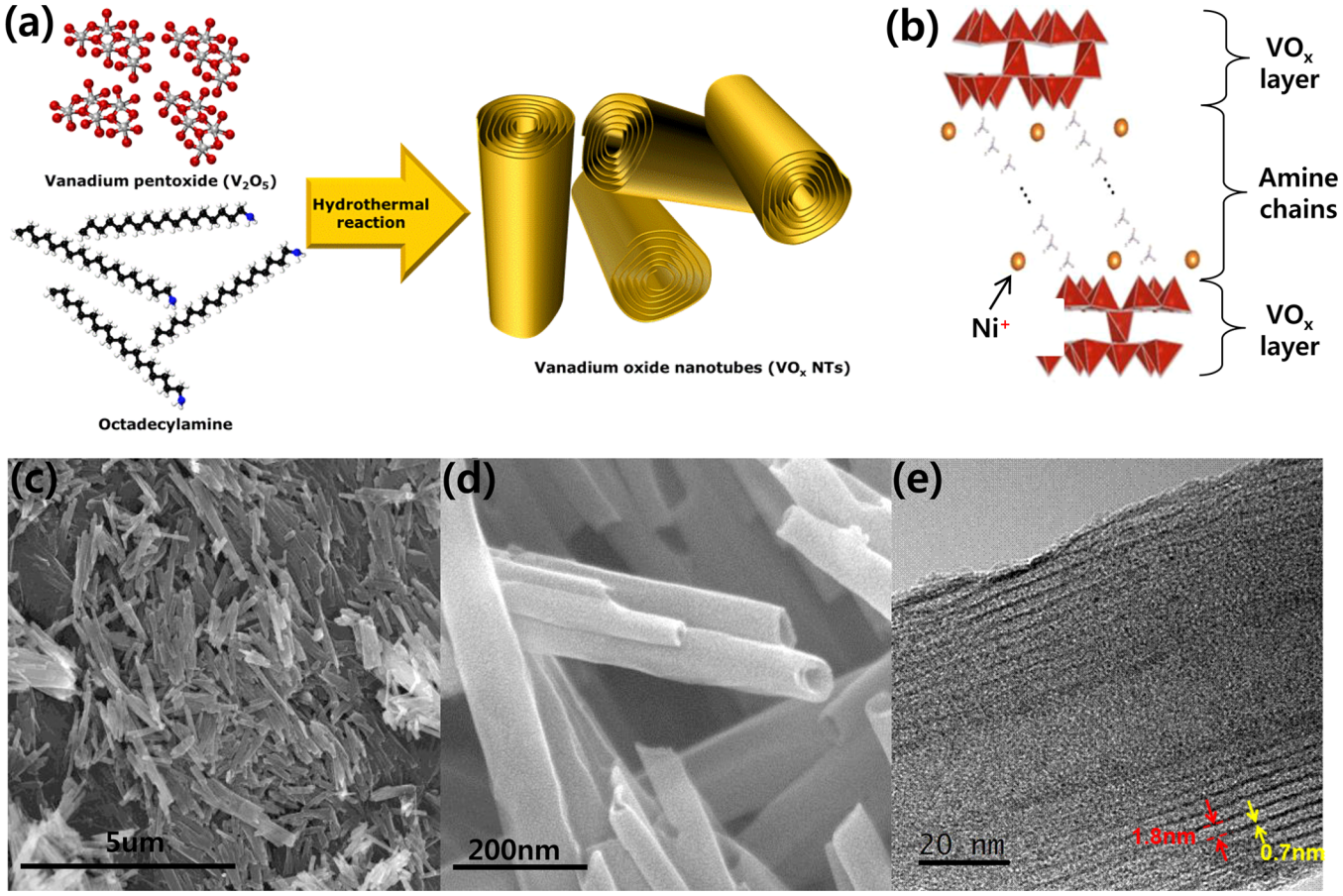

Figure 1. (a) Schematic illustration of hydrothermally synthesized VO_x NTs, (b) schematic illustration of $Ni_{0.1}VO_x$ NTs, (c) low-resolution SEM images of $Ni_{0.1}VO_x$ NTs, (d) high-resolution SEM images of $Ni_{0.1}VO_x$ NTs and (e) high-resolution TEM images of $Ni_{0.1}VO_x$ NTs.

NT cathode showed high initial discharge capacity and relatively low cycle retention. The degradation mechanism was clarified in terms of the structural changes and surface chemistry using TEM, XRD, XPS, and FT-IR analyses and theoretical calculations. It is observed that during discharging, the amine interlayer expands and carbon and oxygen are adsorbed at the $Ni_{0.1}VO_x$ NTs cathode materials. These results were simulated in detail by a first principle study using the ab initio method. The experimental and numerical simulation results suggested that the main structural degradation is caused by solvent-molecule coordinated Na-insertion mechanisms into the relatively fragile amine interlayer during discharging.

2. RESULTS AND DISCUSSION

VO_x NTs were synthesized using a microwave-assisted hydrothermal method. After that, Ni doping has been carried out using a cationic exchange reaction. The detail experimental method and the characterization of Ni-doping effects were described in experimental method sessions and our previous work.[5] Figure 1a illustrates hydrothermally synthesized VO_x NTs using V_2O_5 precursors and amine templates and Figure 1b shows a schematic of the $Ni_{0.1}VO_x$ NTs. $Ni_{0.1}VO_x$ NTs comprise VO_x layers and octadecylamine ($CH_3(CH_2)_{16}CH_2NH_2$) templates, which correspond to the dark and light fringes in the TEM images (Figure 1e).[20] Ni^+ are supposed to be positioned in the space between the VO_x layers with a molar ratio of 1:10 (Ni: V).[5] The structures and morphology of $Ni_{0.1}VO_x$ NTs were investigated by scanning electron microscopy (SEM) and transmission electron microscopy (TEM). Low- and high-resolution SEM images are shown in Figure 1c, d. The high-resolution SEM image in Figure 1d clearly exhibits open-ended, multilayered tubular structures of $Ni_{0.1}VO_x$ NTs, with the outer diameter being ~100 nm. The high-resolution (HR) TEM image in Figures 1e shows that VO_x NTs had a layered structured comprising alternately arranged ~0.7 nm thick VO_x layers (dark fringes) and ~2 nm thick amine layers (broad and light fringes).[21−24]

Figures 2a shows the discharging and charging profiles of the $Ni_{0.1}VO_x$ NTs for the 1st, 5th, 10th, 20th, and 50th cycles with 0.1C rate. The first discharging capacity of the $Ni_{0.1}VO_x$ NTs was 145 mA h g^{-1}. The estimated theoretical reversible capacity for nanostructured $Na_2V_2O_5$ is around 250 mA h g^{-1}, assuming that the anmine layers are inactive in the intercalation. In the first discharging profile, the potential plateau of the $Ni_{0.1}VO_x$ NTs is positioned at ~2.2 V, attributable to Na-ion intercalation processes.[10] After the cycles goes on, the discharge capacities were decreased and plateau region becomes narrower and disappears.

The cyclic voltammogram (in Figure 2b) shows smooth cathodic peaks at around 2.2 and around 1.4 eV, and anodic oxidation peak at around 2.6 eV. These peak positions are well matched with discharging/charging plateaus. Figure 2c shows the capacity retention and efficiency of the $Ni_{0.1}VO_x$ NTs. The $Ni_{0.1}VO_x$ NTs exhibited an efficiency of >98% for up to the 50th cycle, indicating that the intercalated Na^+ were completely extracted from the Ni-doped VO_x NT-based cathode. However, capacity fading was observed after the third cycle. The charge/

DOI: 10.1021/am506051t
ACS Appl. Mater. Interfaces 2015, 7, 1477−1485

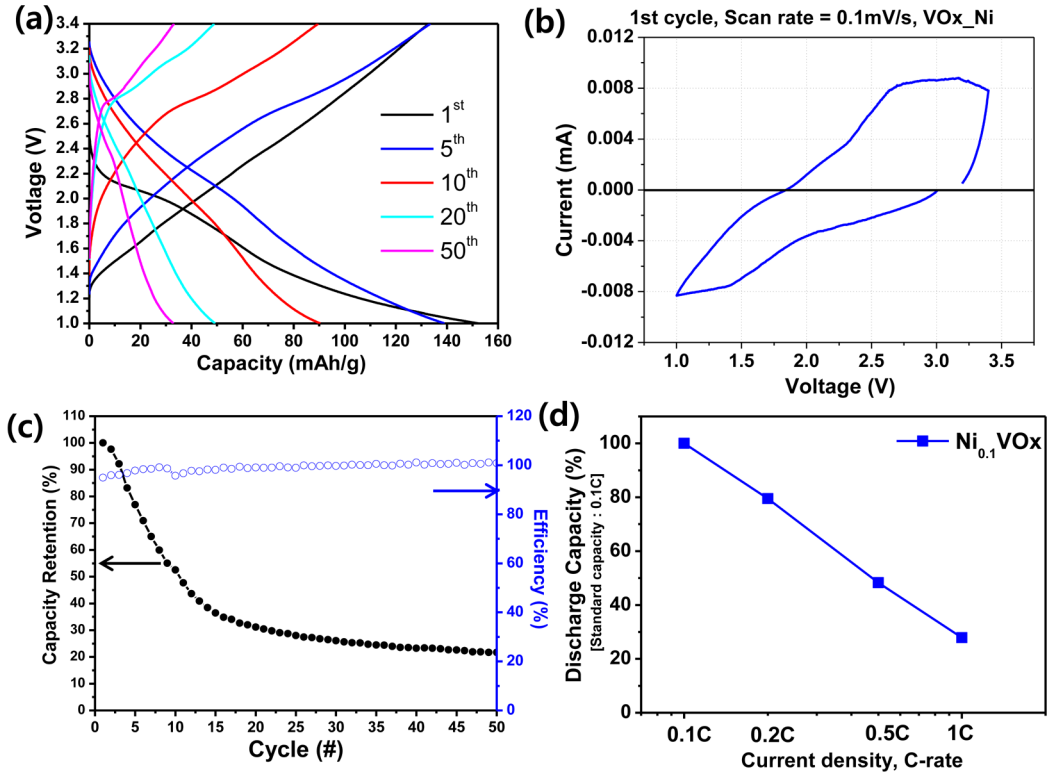

Figure 2. (a) Discharge and charge profiles of the $Ni_{0.1}VO_x$ NTs at 0.1C, (b) cyclic voltammogram with 0.1 mV s scan rate, (c) capacity retention(black square) and efficiency (blue round) of the $Ni_{0.1}VO_x$ NTs at 0.1C, (d) capacity of the $Ni_{0.1}VO_x$ NTs at the different *C* rates.

discharge characteristics were tested with cells cycled at 0.1, 0.2, 0.5, and 1C. With an increase in the *C* rate, the discharge capacity decreased (Figure 2d). This behavior may be attributable to an increase in the overpotential with increased *C* rate, resulting from the lack time for Na-ion intercalation process.[8] Figure 2d shows the capacity vs *C* rate; 50% of capacity was observed when the *C* rate was increased from 0.1 to 0.5*C*.

The structural changes during electrochemical Na intercalation were thoroughly examined through TEM and XRD analyses. The TEM images and XRD patterns of $Ni_{0.1}VO_x$ NTs were taken in three different charging/discharging states: (i) as-prepared electrode, (ii) electrode after full discharging up to 1 V, and (iii) electrode after full charging up to 3.4 V. The TEM images of three electrodes are shown in Figure 3a−c. It is obviously observed that the spacing of amine layers are increased from 2.1 to 4.2 nm after discharging process and recovered back to 2.2 nm after charging process. On the other hands, the spacings from VO_x layers are not significantly changed during discharging/charging processes; changed from 0.7 nm (as-is) to 0.78 nm (discharged), and 0.78 nm (charged). Those significant changes of amine layers were observed in XRD patterns, as well. Figure 3d−f show the XRD patterns of three individual electrochemical states. The XRD patterns show low-angle ($2\theta < 13°$) diffraction peaks from the diffraction of layered structures of $Ni_{0.1}VO_x$ NTs, and high angle ($2\theta > 13°$) diffraction peaks from two-dimensional structures of the VO_x layer. Low-angle diffraction peaks showed obvious peak shifts when the cell was discharged and charged. Originally, the (002) peak of as-prepared $Ni_{0.1}VO_x$ NTs was positioned at 5.5°, and the peak shifted to 4.2° after the first discharging. Then, after the first charging, the (002) peak of $Ni_{0.1}VO_x$ NTs shifted back to 5°. If the peak positions were converted to the interlayer spacing of $Ni_{0.1}VO_x$ NTs, the interlayer spacings (the spacings of VO_x layer plus amine layer) of $Ni_{0.1}VO_x$ NTs in each electrochemical state would be 3.2, 4.2, and 3.5 nm for as-prepared, first discharged, and first charged $Ni_{0.1}VO_x$ NTs, respectively. These results show that during the first discharging, the interlayer spacing of $Ni_{0.1}VO_x$ NTs is expanded up to 1 nm, and during the first charging, it reduces back to the original distance. Moreover, the fwhm of low-angle peaks from the discharged electrode was obviously larger than that of the other two electrodes. On the other hand, significant XRD peak shifts from the first discharging spectra were not observed in the high-angle region ($2\theta > 13°$), where the diffraction peaks from two-dimensional metal oxide structures are assigned. From the first discharging XRD data, the peaks at large-angle regions become slightly broader compared with those from the as-prepared or first charged electrodes. The XRD results showed that the amine interlayer spacings expanded and contracted during Na+ insertion into and extraction from the $Ni_{0.1}VO_x$ NTs, respectively. As shown in Figure 3g, we have additionally taken FT-IR spectra for as-is, discharged, and charged electrodes, respectively. The as-is and charged electrodes show V═O peak at ∼1000 cm^{-1} and other peaks are matched with PVDF, etc. In the discharged electrode, the peaks from 1000 to 700 cm^{-1} are matched with vanadate compounds (VO_4^{-3}). These peak changes from the vanadium oxide region indicates that there were reversible bonding energy or valence states changes during intercalation/deintercalation processes. In addition, from the discharged electrode, the clear carbonate peak is observed at ∼1450 cm^{-1} and disappeared from as-is and charged electrodes, indicatives of reversible accumulation/dissolution of (decomposition of) electrolytes.

DOI: 10.1021/am506051t
ACS Appl. Mater. Interfaces 2015, 7, 1477−1485

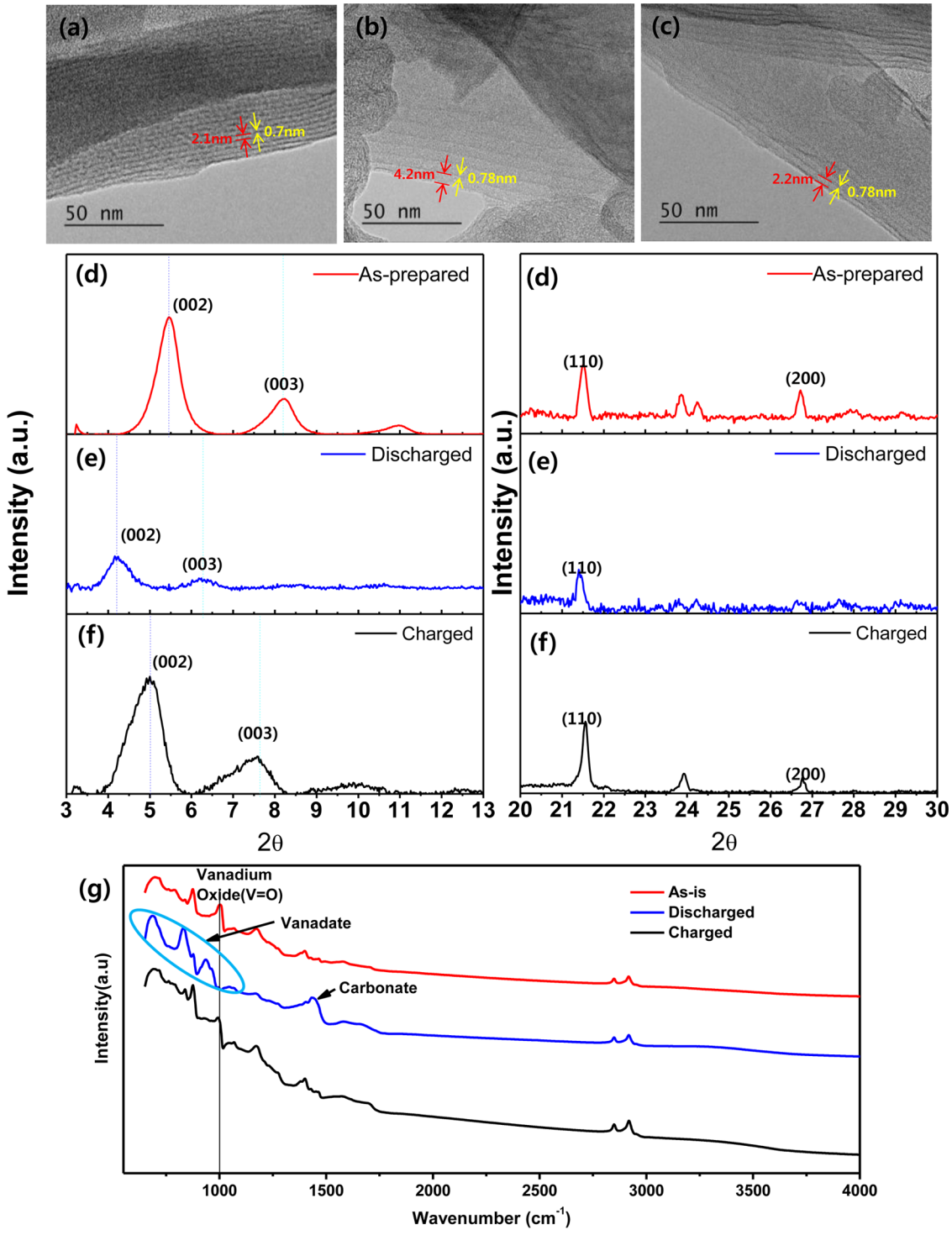

Figure 3. Comparison of TEM images of the $Ni_{0.1}VO_x$ NT electrodes: (a) as-prepared electrode, (b) electrode after discharged, (c) electrode after charged; and comparison of XRD patterns: (d) as-prepared electrode, (e) electrode after discharged, (f) electrode after charged; and (g) comparison of FT-IR spectra of three electrodes.

X-ray photoelectron spectroscopy (XPS) analysis was performed to understand the chemical states of the as-prepared, discharged, and charged $Ni_{0.1}VO_x$ NTs electrodes. To compare the chemical compositions between the surface and the interior regions of $Ni_{0.1}VO_x$ NTs electrodes, we measured core-level spectra for the pristine electrode and electrodes after the first and second Ar^+ sputtering (with 500 V acceleration voltages). All spectra were referenced to the C 1s peak at 284.8 eV. The core level spectra of the as-prepared $Ni_{0.1}VO_x$ NTs electrode, shown in Figure 4a–c, exhibit no significant intensity change after Ar^+ sputtering, indicating uniform mixing with $Ni_{0.1}VO_x$, PVDF, carbon (Ketjen black) and additive residues. The peaks appearing at the lower binding energy side of V 2p and F 1s after Ar^+ sputtering, as shown in Figures 4b, d, could be assigned to metal fluoride and vanadium suboxide, respectively. During discharging, Na^+ was inserted into the $Ni_{0.1}VO_x$ NTs

DOI: 10.1021/am506051t
ACS Appl. Mater. Interfaces 2015, 7, 1477–1485

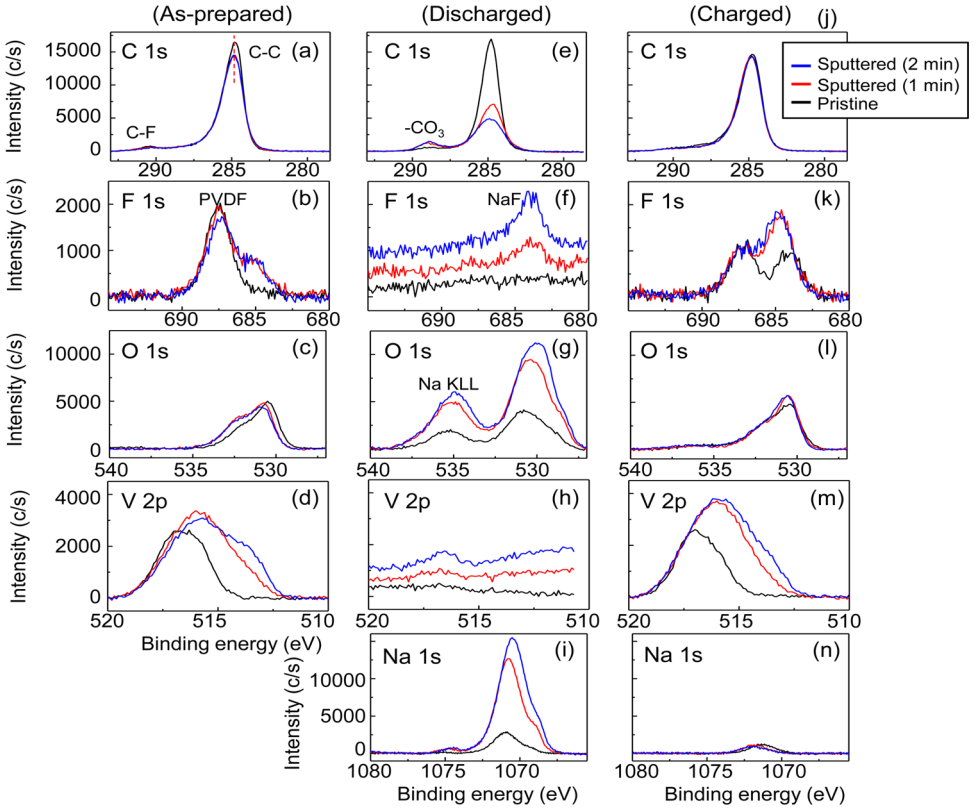

Figure 4. C 1s, F 1s, O 1s, V 2p, and Na 1s core-level spectra for $Ni_{0.1}VO_X$ NT electrode as a function of Ar^+ sputter time. (a–d) As-prepared $Ni_{0.1}VO_X$ NT. (e–i) Discharged $Ni_{0.1}VO_X$ NT. (j–n) Charged $Ni_{0.1}VO_X$ NT.

electrode and formed an SEI layer. Figure 4e–i show that the outer surface of the fully discharged electrode is mainly covered with a carbon-rich layer, which originated from accumulation of carbon species during Na intercalation. After removing this layer, the discharged electrode shows a decomposition species of electrolytes that mainly consists of oxygen, carbon and/or sodium species. The discharged electrode shows higher C, O, and Na contents compared with as-prepared and charged electrodes, which originated from electrolytes or decomposition of electrolytes, including C═O, C–O group. Therefore, the intensity of C 1s in Figure 4e is lower than in the as-prepared sample. However, when compared with the relative carbon concentration in the as-prepared sample, we found that the carbon content at outer surface increases after discharging. The estimated atomic concentrations of three electrodes are shown in the Supporting Information (Table S1). Note here that because of the accumulated layer on the cathode surface during discharging, the peak intensities of V and C from the inner cathode surface were much weaker. The variations of O and C ratio after Ar+ sputtering indicate some degree of electrolytes decompositions. This result indicates that the carbon and oxygen species from propylene carbonate (PC) and decompositions of electrolytes are accumulated on the surface of $Ni_{0.1}VO_x$ NTs, during discharging. The initial phase of the $Ni_{0.1}VO_x$ NTs electrode was recovered by charging, as shown in Figure 4j–n and residual Na^+ forms a carbonate and fluoride on the surface.

To clarify the reaction site of Na^+ in the electrodes during the electrochemical Na insertion processes, we performed a "modeling study" based on ab initio calculations. The Vienna ab initio Software Package (VASP) was used to perform DFT calculations with the generalized gradient approximation (GGA) as parametrized by Perdew, Burke, and Ernzerfhof (PBE) for the exchange-correlation functional. In the experiment, octadecylamine and Ni^+ are incorporated between VO_x layers; On the other hands, in the modeling study, only ethylene diamine cations are incorporated between VO_x layers to simplify the calculations. To treat octadecyleamine cations with a much larger interlayer space between VO_x layers, although it might be more comparable with the experiments, the simulation cost is very expensive, and the crystal structures of VO_x with ethylene diamine cations are known. Thus, the model electrode includes a $V_{14}O_{32}C_4N_4H_{20}$ stoichiometry, which is composed of double V_7O_{16} layers between which ethylene diamine cations are embedded. The single V_7O_{16} layer comprises two sheets of square VO_5 pyramids and VO_4 tetrahedra that connect these sheets.[20]

Two possible Na-insertion pathways are considered. Path 1 is between two V_7O_{16} layers and Path 2, between two sheets of square VO_5 pyramids, as shown in Figure 5a. The minima structures in Figure 5d–f, where Na is inserted via Path 2, are energetically unstable by 0.5, 0.9, and 1.0 eV, respectively, relative to that in Figure 5b, where Na is inserted via Path 1. The probability of existence of structures in Figure 5d–f compared to that in Figure 5b can be deduced by the equilibrium constant K, calculated from the equation $\Delta G = -RT \ln K$, where ΔG is the relative energy; R, the universal gas constant; and T, the temperature, and $K \approx 1 \times 10^{-9}$, 1×10^{-15}, and $\sim 1 \times 10^{-17}$ at 298 K. Moreover, the Na-insertion processes by Path 2 are accompanied by much structural distortion (Figure 5d–f), indicating that the reversible Na insertion and desertion processes are not feasible through Path 2. Thus, the Na-insertion processes occur via Path 1.

DOI: 10.1021/am506051t
ACS Appl. Mater. Interfaces 2015, 7, 1477–1485

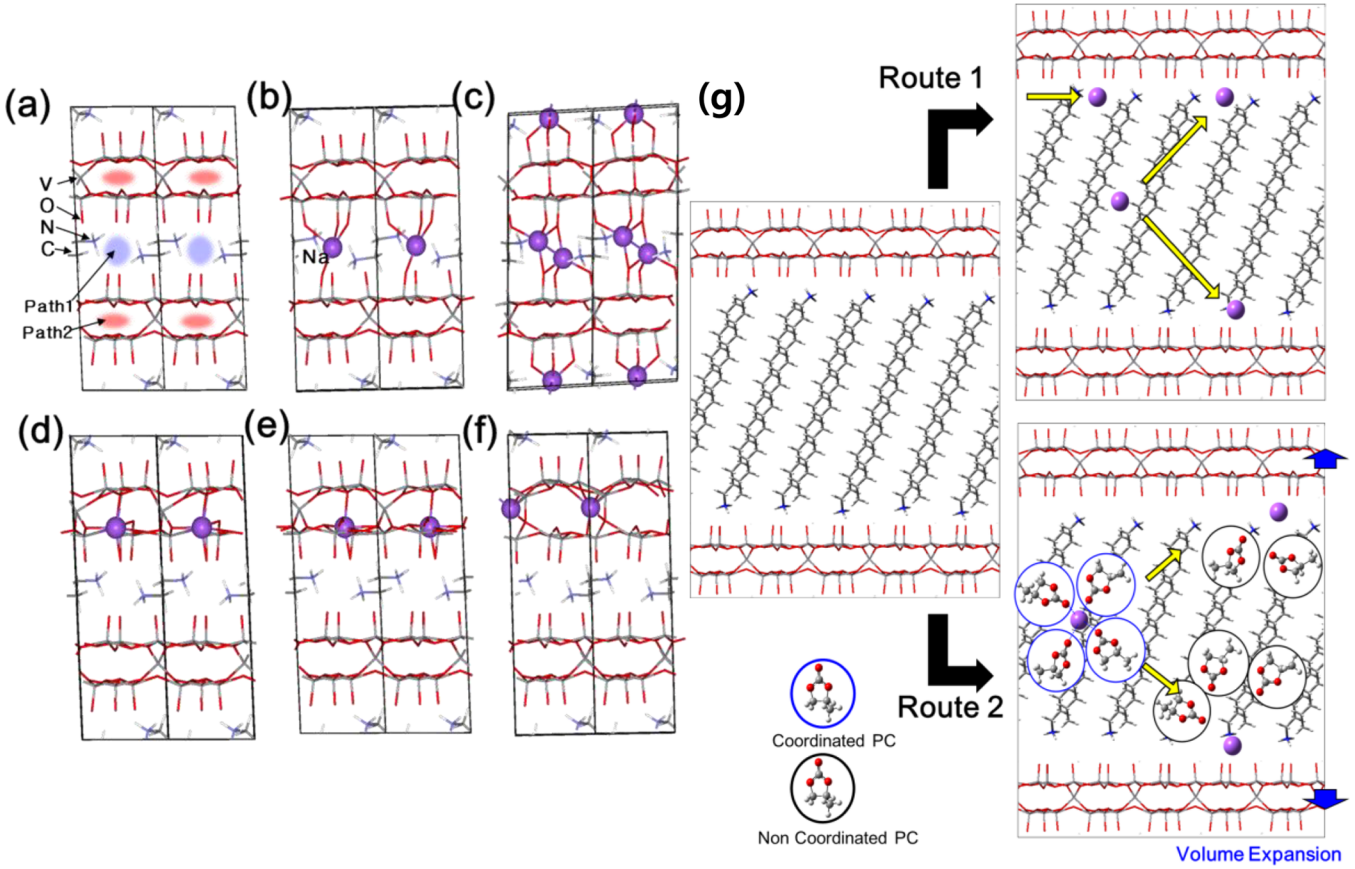

Figure 5. (a) Two possible Na-insertion paths into the model electrode including a $V_{14}O_{32}C_4N_4H_{20}$. (b/c) Single/double Na-insertions via Path1. (d–f) Single Na-insertions via Path2. (g) Schematic view of the PC-uncoordinated/coordinated Na-insertion processes into the VO_x layer (Route1/Route2).

On the other hand, when Na is inserted into the model electrodes (Figure 5a–c), the volumes of cells decrease slightly with the distance decrease between two V_7O_{16} layers. Compared to the structure without Na insertion, shown in Figure 5a, the cell volumes of the Na-inserted structures in Figure 5b, c are ∼1% smaller, which differs from the experimental observations; When Na is experimentally inserted into the $Ni_{0.1}VO_x$ NT electrodes, the distances between the two V_7O_{16} layers where octadecylamine and Ni^+ are incorporated are increased by up to 30% (Figure 3b, e) from the TEM and XRD analyses. Moreover, XPS analysis revealed the accumulation and relaxation of carbon and oxygen species on the VO_x surface during discharging and charging by XPS analysis (Figure 4). More evidently, FT-IR spectra show that strong carbonate peak is appeared after discharged, and disappeared after charged process (Figure 3g). These experimental facts suggest that a significant amount of the solvent molecule-coordinated Na-moieties intercalate into the VO_x layer, as shown by Route 2 in Figure 5g, along with Na^+ intercalation, as shown by Route 1 in Figure 5g, resulting in the large amount of expansion of amine interlayers and the accumulation of carbon and oxygen species at the surface. Thus, it is confirmed that the Na-insertion processes into the $Ni_{0.1}VO_x$ NT electrodes are accompanied by solvent insertion (herein, PC molecules) into the electrodes, as schematically shown in Figure 6, in a manner similar to the previously reported phenomenon in which the solvent coordinated Li[25−27] and Na[28,29] is coinserted into the graphite anodes[25−29] and cathodes.[30] It should be noted that Ni-doped VO_x NTs consist of a layered structure that was composed of alternately arranged VO_x layers (∼0.7 nm) and amine layers (∼2 nm). From the simulation results, the Na+ is inserted into the space between two V_7O_{16} layers, which is enough space for PC coordinated Na ion to be intercalated. Therefore, the cointercalation process of PC-coordinated molecules is possible through large spacing in Ni-dope VO_x NTs structures, differently from other metal oxide cathode materials, which have no enough spaces for the cointercalation of PC coordinated Na ion.

When the cell is discharged, Na^+ is inserted with the coordinated solvent molecules (Step1 in Figure 6). This leads to the accumulations of carbon and oxygen species of solvent molecules in the VO_x electrodes and the expansion of the layered spacing (Step2). In the final step of the Na intercalations, coordinated solvent molecules would be desolvated with the reaction of $PC_nNa^+ + e^- \rightarrow Na + nPC$ (Step3). The expansion of layered spacing with the solvent-coordinating Na-insertion processes produces amine cations, which are unbound to the VO_x layer surface, and thus, PC molecules will interact with amine cations. This increased disorder might accelerate a degradation of the VO_x electrodes. The interaction free energy at 298 K between Na^+ and a PC molecule is −1.3 eV, whereas that between an ethylene diamine cation and a PC molecule is −1.9 eV. Interaction free energies are calculated at the M062*X*/6-311+G** level using Gaissian 09.[31] When the cell charged, Na deserts with coordinating solvent molecules, with decreasing VO_x layer spacing (Figure 3c, f) and disappearing of carbonate peaks (Figure 3g), indicative of reversible reaction. However, some of solvent

DOI: 10.1021/am506051t
ACS Appl. Mater. Interfaces 2015, 7, 1477−1485

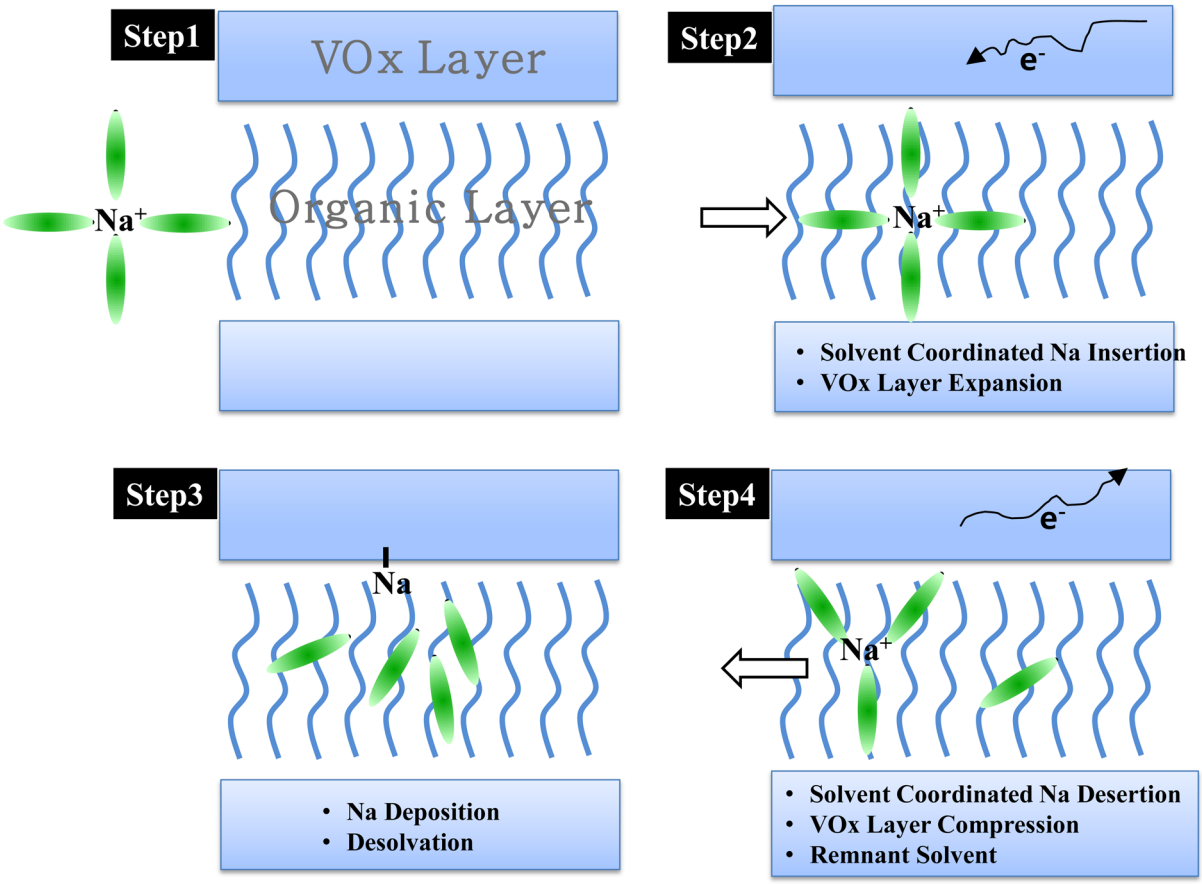

Figure 6. Schematic description of insertion and deinsertion process of solvated Na^+.

molecules can remain inside the VO_x layers (Step4), and these solvent molecules inside the VO_x layers can be oxidized during the charging processes.

The fast capacity fading of the $Ni_{0.1}VO_x$ NTs, as shown in Figure 2b, can be attributed to the solvated Na-intercalation processes for the following reasons. First, structural degradation may occur owing to the stress produced by the intercalation of much larger solvated cations, leading to electrode exfoliation and rupture. Second, solvent molecules are oxidized in the organic layers inside VO_x electrodes as well as on the electrode surface. The intermediates and products of oxidized solvent molecules can undergo other reactions which can degrade organic layers within the VO_x structures. Third, large cracks can be formed on the SEI surface on the VO_x electrodes owing to the large volume change, and the reformation process of the SEI layer continues to consume additional electrolytes and charges. These understandings of the Na intercalation process would be useful for improving the fast capacity fading effects of $Ni_{0.1}VO_x$ NT electrodes in a Na battery.

3. CONCLUSION

In this study, we have successfully utilized $Ni_{0.1}VO_x$ nanotubes (NTs) as a cathode material for a Na ion battery. Toward this end, VO_x NTs were synthesized by a microwave-assisted hydrothermal process, and Ni doping was performed by a cationic exchange reaction. The produced $Ni_{0.1}VO_x$ NT cathode showed high initial discharge capacity up to 140 mAh/g. Moreover, its structural evolution and surface chemistry were examined during the discharging and charging processes. The structural expansion/contraction and surface accumulation/relaxation of carbon species were observed by TEM, XRD, FT-IR, and XPS analyses.

These results were thoroughly simulated by a first-principles study using the ab initio method. Based on the simulation and experimental results, it was proposed that the solvent molecules coordinated the Na-insertion mechanisms into the amine interlayer during discharging. This effect is considered one of the main reasons for fast capacity fading in VO_x NT electrodes applied to a Na-ion battery.

4. EXPERIMENTAL METHODS

4.1. Synthesis of Ni-Doped VO_x Nanotubes. VO_x NTs were synthesized using a microwave-assisted hydrothermal method: 0.91 g (0.05 mol) of V_2O_5 and 1.35 g (0.05 mol) of octadecylamine were stirred into 5 mL of ethanol for 1 h. Then, 15 mL of water was added to the solution. The precursor solution was magnetically stirred for 48 h to obtain a homogeneous mixture. This mixture was placed in a Teflon-lined autoclave and heated at 180 °C for 18 h using a Mars 6 microwave. The final products were stirred in ethanol for 40 h to wash the residue and were subsequently filtered. The obtained VO_x powders were then heated in a convection oven at 80 °C for 12 h.

Ni-doped VO_x NTs were obtained using a cationic exchange reaction. 5.7 g of $NiCl_2$ was dissolved in 20 mL of deionized water. Then, 1 g of the synthesized VO_x NTs was dispersed in a solution of deionized water/absolute ethanol (volume ratio of 1:8), and the dispersion was stirred using a magnetic bar. The $NiCl_2$ solution and the dispersion of the VO_x NTs were mixed and stirred at 30 °C for 20 h. The final product was rinsed and filtered. The thus-obtained powder was dried in a vacuum oven at 80 °C for 12 h and then heated in the oven for 2 h.

4.2. Sample Characterization. XRD analyses were performed using Cu Kα radiation for 2θ values of 3−55°; the scan rate was 0.02°

DOI: 10.1021/am506051t
ACS Appl. Mater. Interfaces 2015, 7, 1477−1485

min^{-1}. The applied potential and current was 40 kV and 40 mA, respectively. XPS analysis was performed using a Quantum 2000 Scanning ESCA microprobe system (Physical Electronics Instruments) with focused monochromatized Al Kα radiation (1486.6 eV). The morphologies of the Ni-doped VO_x NTs were investigated using a Hitachi S-4700N SEM.

4.4. Electrochemical Measurements. $Ni_{0.1}VO_x$ electrodes were prepared by slurry casting. The electrodes were composed of 60 wt % active material, 20 wt % Ketjen black, and 20 wt % polyvinylidene difluoride. The composite was pasted on an aluminum foil current collector, dried at 120° in vacuum, and then pressed. Metallic Na was used as the anode. To synthesize the electrolyte, 1 mol L^{-1} $NaPF_6$ was dissolved in propylene carbonate. Glass fibers were used as the separator. R2032-type coin cells were assembled in an Ar-filled glovebox. Cyclic voltammetry (model VMP3, NanoQuébec) was performed at a scan rate of 10 $\mu V\ s^{-1}$. For the galvanostatic experiments, the cells were discharged/charged at constant current.

■ ASSOCIATED CONTENT

Supporting Information

Estimated atomic concentrations of as-is, discharging and charging electrodes of Ni-doped VO_x NTs with respect to Ar+ sputtering. This material is available free of charge via the Internet at http://pubs.acs.org/.

■ AUTHOR INFORMATION

Corresponding Author

*E-mail: ydmj79.park@samsung.com. Tel.: +82-31-8061-1250. Fax: +82-31-8061-1319.

Notes

The authors declare no competing financial interest.

■ ACKNOWLEDGMENTS

This work was supported by the Samsung Advanced Institute of Technology.

■ REFERENCES

(1) Berthelot, R.; Carlier, D.; Delmas, C. Electrochemical investigation of the P2-Na_xCoO_2 phase diagram. *Nat. Mater.* **2011**, *10*, 74−80.

(2) Palomares, V.; Serras, P.; Villaluenga, I.; Hueso, K. B.; Carretero-González, J.; Teófilo, R. Na-ion batteries, recent advances and present challenges to become low cost energy storage system. *Energy Environ. Sci.* **2012**, *5*, 5884−5901.

(3) Yoo, H. D.; Shterenberg, I.; Gofer, Y.; Gershingsky, G.; Pour, N.; Aurbach, D. Mg rechargeable batteries: an on-going challenge. *Energy Environ. Sci.* **2013**, *6*, 2265−2279.

(4) Kim, H. S.; Arthur, T. S.; Allred, G. D.; Zajicek, J.; Newman, J. G.; Rodnyansky, A. E.; Oliver, A. G.; Boggess, W. C.; Muldoon, J. Structure and compatibility of a magnesium electrolyte with a sulphur cathode. *Nat. Commun.* **2011**, *2*, 427.

(5) Kim, H.; Kim, R.-H.; Lee, S.-S.; Kim, Y.; Kim, D.-Y.; Park, K. Effects of Ni doping on the initial electrochemical performance of vanadium oxide nanotubes for Na-ion batteries. *ACS Appl. Mater. Interfaces.* **2014**, *6*, 11692−11697.

(6) Operating mechanisms of electrolytes in magnesium ion batteries: chemical equilibrium, magnesium deposition, and electrolyte oxidation Phys. Chem. Chem. Phys., 2014, DOI: 10.1039/C4CP01259C.

(7) Hamani, D.; Ati, M.; Tarascon, J.-M.; Rozier, P. Na_xVO_2 as possible electrode for Na-ion batteries. *Electrochem. Commun.* **2011**, *11*, 938−941.

(8) Fei, H.; Liu, X.; Lin, Y.; Wei, M. Facile synthesis of ammonium vanadium oxide nanorods for Na-ion battery cathodes. *J. Colloid Interface Sci.* **2014**, *428*, 73−77.

(9) Tepavcenvic, S.; Xiong, H.; Stamenkovic, V. R.; Zuo, X.; Balasubramania, M.; Prakapenka, V. B.; Johnson, C. S.; Rajh, T. Nanostructured bilayered vanadium oxide electrodes for rechargeable sodium-ion batteries. *ACS Nano* **2012**, *6*, 530−538.

(10) Su, D.; Wang, G. Single-crystalline bilayered V_2O_5 nanobelts for high-capacity sodium-ion batteries. *ACS Nano* **2013**, *7*, 11218−11226.

(11) Rui, X.; Lu, Z.; Yu, H.; Yang, D.; Hng, H. H.; Lim, T. M.; Yan, Q. Ultrathin V_2O_5 nanosheet cathodes: Realizing ultrafast reversible lithium storage. *Nanoscale* **2013**, *5*, 556−560.

(12) Lee, J. W.; Lim, S. Y.; Jeong, H. M.; Hwang, T. H.; Kang, J. K.; Choi, J. W. Extremely stable cycling of ultra-thin V_2O_5 nanowire-graphene electrodes for lithium rechargeable battery cathodes. *Energy Environ. Sci.* **2012**, *5*, 9889−9894.

(13) Qu, Q.; Zhu, Y.; Gao, X.; Wu, Y. Core-shell structure of polypyrrole grown on V_2O_5 nanoribbon as high performance anode material for supercapacitors. *Adv. Energy Mater.* **2012**, *2*, 950−955.

(14) Jiao, L.; Yuan, H.; Wang, Y.; Cao, J.; Wang, Y. Mg intercalation properties into open-ended vanadium oxide nanotubes. *Electrochem. Commun.* **2005**, *7* (4), 431−436.

(15) Zhou, X.; Wu, G.; Gao, G.; Wang, J.; Yang, H.; Wu, J.; Shen, J.; Zhou, B.; Zhang, Z. Electrochemical performance improvement of vanadium oxide nanotubes as cathode materials for lithium ion batteries through ferric ion exchange technique. *J. Phys. Chem. C* **2012**, *116*, 21685−21692.

(16) Vera-Robles, L. I.; Naab, F. U.; Campero, A.; Duggan, J. L.; McDaniel, F. D. Metal cations inserted in vanadium-oxide nanotubes. *Nucl. Instrum. Methods Phys. Res., Sect. B* **2007**, *261* (1), 534−1537.

(17) Reinoso, J. M.; Muhr, H. J.; Krumeich, F.; Bieri, F.; Nesper, R. Controlled uptake and release of metal cations by vanadium oxide nanotubes. *Helv. Chim. Acta* **2000**, *83*, 1724−1733.

(18) Nordlinder, S.; Lindgren, J.; Gustafsson, T.; Edström, K. The structure and electrochemical performance of Na^+-, K^+-, and Ca^{2+}-vanadium oxide nanotubes. *J. Electrochem. Soc.* **2003**, *150* (5), E280−E284.

(19) Nordlinder, S.; Edström, K.; Gustafsson, T. The performance of vanadium oxide nanorolls as cathode material in a rechargeable lithium battery. *Electrochem. Solid-State Lett.* **2001**, *4*, A129−A131.

(20) Wörle, M.; Krumeich, F.; Bieri, F.; Muhr, H. J.; Nesper, R. Flexible V_7O_{16} layers as the common structural element of vanadium oxide nanotubes and a new crystalline vanadate. *Z. Anorg. Allg. Chem.* **2002**, *628*, 2778−2784.

(21) Leroy, S.; Martinez, H.; Dedryvère, R.; Lemordant, D.; Gonbeau, D. Influence of the lithium salt nature over the surface film formation on a graphite electrode in Li-ion batteries: An XPS study. *Appl. Surf. Sci.* **2007**, *253*, 4895−4905.

(22) Park, K.; Han, D.; Kim, H.; Chang, W.; Choi, B.; Anass, B.; Lee, S. Characterization of a P_2-type chelating-agent-assisted $Na_{2/3}Fe_{1/2}Mn_{1/2}O_2$ cathode material for sodium-ion batteries. *RSC Adv.* **2014**, *43*, 22798−22802.

(23) Hou, X.; Wu, G.; Gao, G.; Cui, C.; Yang, H.; Shen, J.; Zhou, B.; Zhang, Z. The synthesis, characterization and electrochemical properties of multi-wall carbon nanotube-induced vanadium oxide nanosheet composite as a novel cathode material for lithium ion batteries. *Electrochim. Acta* **2012**, *4*, 32−38.

(24) Gies, A.; Pecquenard, B.; Benayad, A.; Martinez, H.; Gonbeau, D.; Fuess, H.; Levasseur, A. Effect of silver co-sputtering on V_2O_5 thin films for lithium microbatteries. *Thin Solid Films* **2008**, *516*, 7271−7281.

(25) Winter, M.; Besenhard, J. O.; Spahr, M. E.; Novák, P. Insertion electrode materials for rechargeable lithium batteries. *Adv. Mater.* **1998**, *10*, 725−763.

(26) Daniel, C.; Besenhard, J. O. *Handbook of Battery Materials*; Wiley−VCH: Weinheim, Germany, 2008; Vol. *1*, pp 495−510

(27) Tasakia, K.; Goldberg, A.; Winter, M. On the difference in cycling behaviors of lithium-ion battery cell between the ethylene carbonate- and propylene carbonate-based electrolytes. *Electrochim. Acta* **2011**, *56*, 10424−10435.

(28) Kim, H.; Hong, J.; Park, Y.-U.; Kim, J.; Hwang, I.; Kang, K. Sodium Storage Behavior in Natural Graphite using Ether-based Electrolyte Systems. *Adv. Funct. Mater.* **2014**, DOI: 10.1002/adfm.201402984.

DOI: 10.1021/am506051t
ACS Appl. Mater. Interfaces 2015, 7, 1477−1485

(29) Jache, B.; Adelhelm, P. Use of graphite as a highly reversible electrode with superior cycle life for sodium-ion batteries by making use of co-intercalation phenomena. *Angew. Chem.* **2014**, *53*, 10169−10173.
(30) Electrochemical Cointercalation of Propylene Carbonate with Alkali Metals in SnS2 Single Crystals. *J. Electrochem. Soc.* **1999**, *146*, 657−662.
(31) Frisch, M. J.; Trucks, G. W.; Schlegel, H. B.; Scuseria, G. E.; Robb, M. A.; Cheeseman, J. R.; Scalmani, G.; Barone, V.; Mennucci, B.; Petersson, G. A.; Nakatsuji, H.; Caricato, M.; Li, X.; Hratchian, H. P.; Izmaylov, A. F.; Bloino, J.; Zheng, G.; Sonnenberg, J. L.; Hada, M.; Ehara, M.; Toyota, K.; Fukuda, R.; Hasegawa, J.; Ishida, M.; Nakajima, T.; Honda, Y.; Kitao, O.; Nakai, H.; Vreven, T.; Montgomery, J. A., Jr.; Peralta, J. E.; Ogliaro, F.; Bearpark, M.; Heyd, J. J.; Brothers, E.; Kudin, K. N.; Staroverov, V. N.; Kobayashi, R.; Normand, J.; Raghavachari, K.; Rendell, A.; Burant, J. C.; Iyengar, S. S.; Tomasi, J.; Cossi, M.; Rega, N.; Millam, M. J.; Klene, M.; Knox, J. E.; Cross, J. B.; Bakken, V.; Adamo, C.; Jaramillo, J.; Gomperts, R.; Stratmann, R. E.; Yazyev, O.; Austin, A. J.; Cammi, R.; Pomelli, C.; Ochterski, J. W.; Martin, R. L.; Morokuma, K.; Zakrzewski, V. G.; Voth, G. A.; Salvador, P.; Dannenberg, J. J.; Dapprich, S.; Daniels, A. D.; Farkas, O.; Foresman, J. B.; Ortiz, J. V.; Cioslowski, J.; Fox, D. J. *Gaussian 09*, revision D.01; Gaussian, Inc.: Wallingford, CT, 2009.

DOI: 10.1021/am506051t
ACS Appl. Mater. Interfaces 2015, 7, 1477−1485